

Impact of Mid- and Upper-Level Dry Air on Tropical Cyclone Genesis and Intensification: A Modeling Study of Durian (2001)

Yaping WANG^{1,3}, Yongjie HUANG^{1,3}, and Xiaopeng CUI^{*1,2,3}

¹*Key Laboratory of Cloud-Precipitation Physics and Severe Storms, Institute of Atmospheric Physics, Chinese Academy of Sciences, Beijing 100029, China*

²*Collaborative Innovation Center on Forecast and Evaluation of Meteorological Disasters, Nanjing University of Information Science & Technology, Nanjing 210044, China*

³*University of Chinese Academy of Sciences, Beijing 100049, China*

(Received 10 February 2018; revised 25 May 2018; accepted 15 June 2018)

ABSTRACT

The impact of mid- and upper-level dry air, represented by low relative humidity (RH) values, on the genesis of tropical cyclone (TC) Durian (2001) in the South China Sea was investigated by a series of numerical experiments using the Weather Research and Forecasting model. The mid-level RH was lowered in different regions relative to TC Durian (2001)'s genesis location. Results suggest that the location of dry air was important to Durian (2001)'s genesis and intensification. The rapid development of the TC was accompanied by sustained near-saturated mid- and upper-level air, whereas low humidity decelerated its development. Water vapor budget analysis showed that moisture at mid and upper levels was mainly supplied by the vertical convergence of moisture flux and the divergence terms, and consumed by the condensation process. The horizontal convergence of moisture flux term supplied moisture in the air moistening process but consumed moisture in the air drying process. With a dryer mid- and upper-level environment, convective and stratiform precipitation were both inhibited. The upward mass fluxes and the diabatic heating rates associated with these two precipitation types were also suppressed. Generally, convection played the dominant role, since the impact of the stratiform process on vertical mass transportation and diabatic heating was much weaker. The vorticity budget showed that the negative vorticity convergence term, which was closely related to the inhibited convection, caused the vorticity to decrease above the lower troposphere in a dryer environment. The negative vorticity tendency is suggested to slow down the vertical coherence and the development rate of TCs.

Key words: tropical cyclone formation, mid- and upper-level dry air, WRF, water vapor budget, convective and stratiform precipitation

Citation: Wang, Y. P., Y. J. Huang, and X. P. Cui, 2018: Impact of mid- and upper-level dry air on tropical cyclone genesis and intensification: A modeling study of Durian (2001). *Adv. Atmos. Sci.*, **35**(12), 1505–1521, <https://doi.org/10.1007/s00376-018-8039-0>.

1. Introduction

Tropical cyclones (TCs) are one of the most destructive weather systems in the world. They usually cause tremendous socioeconomic loss when moving close to coastlines or making landfall at densely populated locations. In particular, those TCs that generate very close to coastlines should be studied more closely, owing to the element of surprise and lack of time to prepare for landfall or to evacuate. The South China Sea (SCS), despite being relatively small in size, is a major TC formation region (Kim et al., 2011). Statistical analyses show that, each year, around 6 or 7 TCs form over the SCS (Wang et al., 2013), and they usually exhibit

the characteristics of rapid development, modest maximum intensity, and a short life cycle (Yi et al., 2008). Although the TCs forming in the SCS are typically weaker than others generating over the Northwest Pacific Ocean, they tend to develop close to land, leading to shorter warning times and increasing the difficulty of timely and accurate forecasts (Lau et al., 2003). Park et al. (2015) pointed out that, once a TC generates, it may move to the west or north and make landfall on the Asian continent within just three days. Thus, predicting the timing and location of TC genesis over the SCS is extremely important, but full of challenges (Nolan, 2007; Park et al., 2015). Understanding the physical processes and mechanisms controlling TC genesis is one of the key objectives of the study reported here.

TC genesis, usually involving multiple physical processes with different spatial and temporal scales, has been studied

* Corresponding author: Xiaopeng CUI
Email: xpcui@mail.iap.ac.cn

by scientists for several decades. Gray (1968, 1977, 1979) proposed six parameters as the large-scale climatological conditions favorable for TC formation: displacement away from the equator; low-level relative vorticity; weak vertical wind shear; sufficient ocean thermal energy with sea surface temperatures greater than 26°C; a deep layer of conditional instability; and high relative humidity (RH) in the mid-troposphere. Among them, environmental humidity plays indispensable roles. Gray (1977) suggested that, when mid-level RH over the ocean is less than 60%, cumulus convection does not typically occur; and when RH is less than 40%, cyclonic development is not possible. Emanuel et al. (2004) found that increased (reduced) mid-tropospheric RH can enhance (suppress) the intensity of storms in sheared environments. The increase of RH in the mid-troposphere can suppress the evaporation of rain (Rotunno and Emanuel, 1987; Emanuel, 1989), further increase the sea surface fluxes, and overcome the negative effect of downdrafts (Bister and Emanuel, 1997), which are beneficial to TC genesis. Observational analyses show that developing tropical disturbances exhibit higher humidity in the mid-troposphere than non-developing ones (Komaromi, 2013; Zawislak and Zipser, 2014). Raymond et al. (1998), based on observations from the Tropical Experiment in Mexico also found that an increase in mid-level RH appears to suppress the development of convective downdrafts, eventually leading to low-level convergence. Bister (2001) revealed that a mid-level mesoscale vortex will intensify when the RH in the mid-troposphere reaches a value of 90%. When the RH in the core exceeds 80% over most of the depth of the troposphere, a mid-level mesoscale convective vortex (MCV) forms, and the intensified MCV causes a more efficient conversion rate from latent heat to kinetic energy in the cyclonic circulation (Nolan, 2007).

On the other hand, dry-air intrusion has been investigated as a potential factor inhibiting TC formation. Many previous studies have examined the suppression of Atlantic hurricane formation and intensification by the intrusion of a Saharan air layer, which is an elevated mixed layer of warm and dry air (Dunion and Velden, 2004; Wu, 2007; Braun et al., 2010; Braun et al., 2012). Emanuel et al. (2008) pointed out that greater sub-saturation of the mid-levels would lead to a longer incubation period for TC formation, as convective episodes moisten the mid-troposphere. Davis and Ahijevych (2012) and Fritz and Wang (2013) found that dry-air intrusion to the lower-to-middle tropospheric wave pouch in a TC suppressed deep convection and redevelopment of the TC. Yoshida et al. (2017) conducted a sensitivity experiment and found that, despite the existence of mid- and low-level vortices, the disturbance did not develop into a TC, because of low water vapor content. When the water vapor content was increased, continuous convection supported persistent upright vortices. Ge et al. (2013) further pointed out that the position of dry air relative to vertical shear determines the impact on TC development. Besides, the latent heating associated with water vapor condensation is a major source of potential energy, which can further convert to kinetic energy

in the tangential wind of the initial TC vortex (Wang et al., 2016a).

During TC formation, convective and stratiform cloud usually develop and exhibit different vertical motions, dynamical and thermodynamic structures, which play important roles in building or maintaining secondary circulations (Fritz et al., 2016). The low-level inflow of the transverse circulation that spins up the near-surface circulation is usually associated with convection, while the mid- to upper-level inflow and the cyclonic circulation are associated with the stratiform process (Wang et al., 2010; Wang, 2012). Also, several studies have emphasized the moistening by convective episodes in the low-to-mid-level environment (Montgomery et al., 2006; Nolan, 2007; Emanuel et al., 2008) or suppression of deep convection by saturation deficit (Rappin et al., 2010; Fritz and Wang, 2013) during TC formation, but the stratiform process has been paid less attention.

The purpose of this study is to explore the genesis process of TC Durian (2001) in the monsoon trough of the SCS under conditions of different mid- or upper-level RH. Two questions are to be answered in this study: Will a TC form with different initial low RH (dry air) regimes in specific storm-relative locations? And how will the convective and stratiform precipitation respond to dry air, and impact TC formation and further intensification? Following this introduction, section 2 presents a brief introduction of TC Durian (2001), including its genesis process. The model configuration and design of the sensitivity experiments are described in section 3, and the results of the experiments are presented in section 4. Section 5 describes the respective characteristics of convective and stratiform cloud in environments with different moisture, and their contributions to the development of the TC. A summary and conclusions are provided in the final section.

2. TC Durian (2001) and its formation process

TC Durian (2001) initially formed as a tropical depression at 0600 UTC 29 June 2001 in the monsoon trough over the SCS. It then moved northwestwards and gradually intensified into a typhoon within 54 hours before its landfall at Guangdong, China, causing considerable damage to South China with heavy rainfall and strong winds (Zhang et al., 2008). Durian's genesis location was rather close to the coastline, and made landfall within three days after its formation.

The origin of Durian (2001) was closely related to the monsoon trough. At 1800 UTC 28 June 2001 (Fig. 1a), the monsoon trough dominated the low-level circulation, and weak positive relative vorticity located at its southern portion. Then, an elongated vortex gradually formed at the southern end of the monsoon trough in the following six hours (Fig. 1b). From 0600 UTC 29 June, the elongated vortex developed into a relatively axisymmetric vortex, with more independent circulation from the monsoon trough and stronger positive relative vorticity (Figs. 1c and d). Based on geostationary meteorological satellite cloud imagery, Zhang et al. (2008) and Wang et al. (2016b) pointed out that the incipient cloud

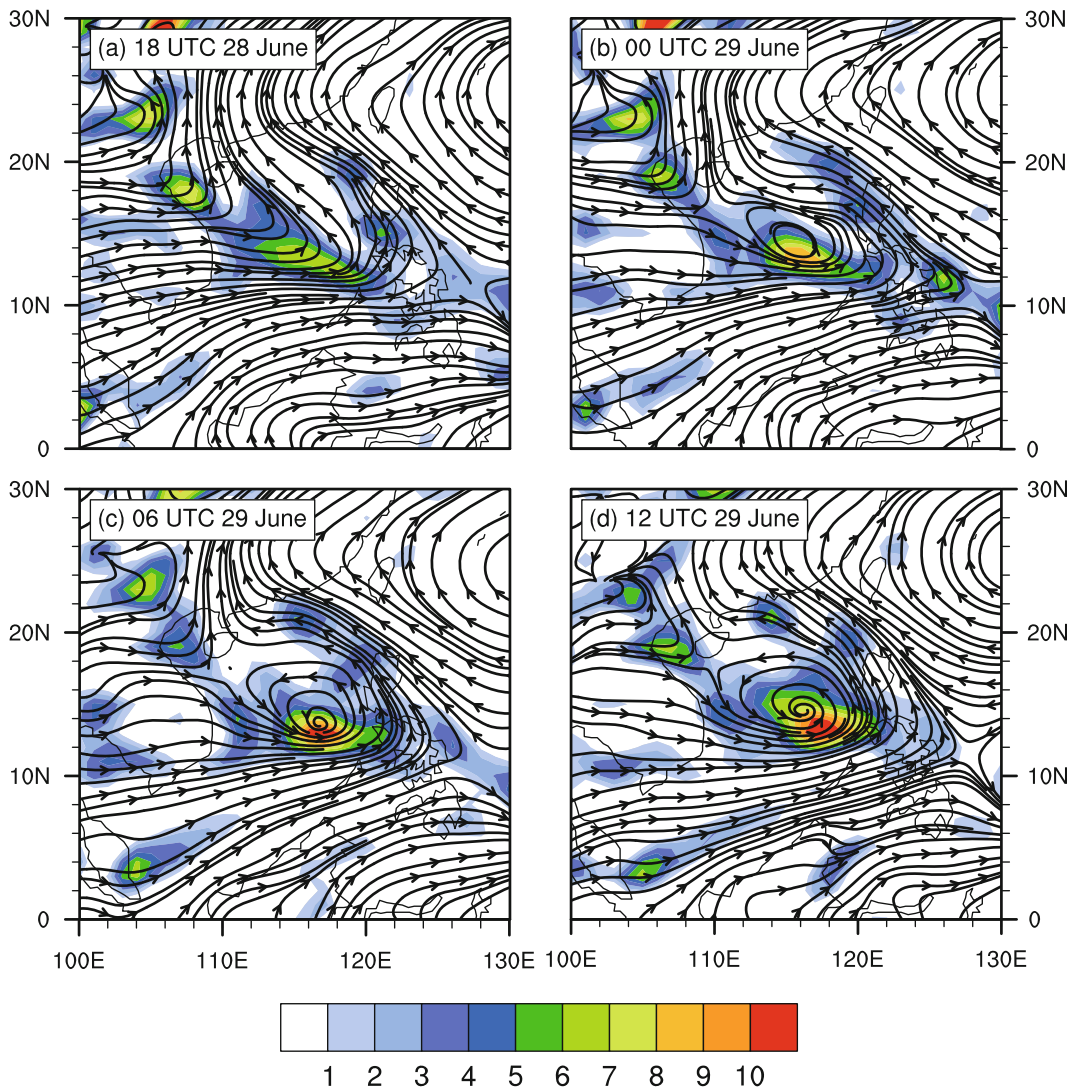


Fig. 1. The 850-hPa horizontal streamlines and relative vorticity (color-shaded; units: 10^{-5} s^{-1}) obtained from the FNL $1^\circ \times 1^\circ$ analysis during the formation of TC Durian (2001), six-hourly, from 1800 UTC 28 June 2001 to 1200 UTC 29 June.

system of Durian could be tracked back to a cloud cluster isolated from pre-existing mature mesoscale convective systems (MCSs).

3. Model configuration and experimental design

The formation process of Durian (2001) in the SCS was successfully simulated by the Weather Research and Forecasting (WRF) model using four nested domains, with the highest resolution being 1.2 km (Wang et al., 2016b). Only the outermost domains, with horizontal resolutions of 54, 18 and 6 km [mesh grids of 112×145 , 235×223 and 373×289 km (Wang et al., 2016b, Fig. 1a)] were used in this study as the control (CTL) experiment, because the 1.2-km resolution domain was not big enough. The outer two domains, with horizontal resolutions of 54 and 18 km, were two-way interactive-nested. The innermost domain, with a horizon-

tal resolution of 6 km, was one-way nested in the 18-km-resolution domain, which meant that the third domain and second domain ran separately. The Goddard microphysics scheme (Tao et al., 1989) and Yonsei University boundary layer scheme (Hong et al., 2006) were used in each domain, while the Kain–Fritsch cumulus parameterization scheme (Kain, 2004) was only used in the outermost two domains. The model integrated from 0000 UTC 28 June to 1200 UTC 01 July 2001 (84 hours) without a bogus vortex, driven by National Centers for Environmental Prediction (NCEP) reanalysis data on $2.5^\circ \times 2.5^\circ$ grids. The integration covered almost the whole lifetime of Durian before its landfall. After about 30 hours' integration, the initial vortex of Durian (2001) generated. The third domain started integration 12 hours after the initial time, for the purpose of saving computing resources and allowing the environment to develop in the outer domains before looking at the highest-resolution domain.

In order to investigate the impact of dry-air intrusion on

TC genesis, a series of sensitivity experiments were conducted, by modifying the initial (at 0000 UTC 28 June 2001) value of RH in the outermost two domains in the mid- and upper troposphere (Table 1). Figure 2 shows the RH distributions at the initial time in all experiments. When we conducted the high-resolution numerical simulation of the CTL experiment (Wang et al., 2016b), high RH greater than 90% at about $(10^{\circ}\text{N}, 116^{\circ}\text{E})$ in the initial condition (Fig. 2a) was one of the major determinant factors in successfully reproducing Durian's genesis timing and location. Thus, the location of the high RH area was denoted as the key area hereafter. In RH-M, the initial mid-level (750–450 hPa) RH was reduced (Fig. 2b). Additionally, the other four experiments were conducted to investigate the impacts of dry air from the upper level (RH-H; 450–150 hPa; Fig. 2c) of the key area, and from surrounding mid-level areas: in the upstream southwest flow of the monsoon trough (RH-SW), in the upstream west flow of the monsoon trough (RH-W), and to the east of the monsoon trough (RH-E), respectively (Figs. 2d–f and Table 1).

The RH modification was based on the original distribution of RH in order to avoid boundary problems. Firstly, we select an elliptical area denoted by

$$|\text{PF1}| + |\text{PF2}| = L, \quad (1)$$

where PF1 and PF2 are the distances between the points on the edge of the ellipse and the two focal points of the ellipse, respectively. In RH-SW, RH-W and RH-E, the focal points

Table 1. Initial RH in the sensitivity experiments.

Experiment name	Description
RH-M	Modified RH value in the central SCS to less than 10% between 750–450 hPa
RH-H	Modified RH value in the central SCS to less than 10% between 450–150 hPa
RH-SW	Modified RH values in the southwesterly flow of the key area, with RH less than 10% in the center and gradually increased with increasing distance to the center between 750–450 hPa
RH-W	Similar to RH-SW but the dry air region is in the westerly flow
RH-E	Similar to RH-W but the dry air region is in the east of the key area

of the ellipse area are $[(6^{\circ}\text{N}, 110^{\circ}\text{E}), (6^{\circ}\text{N}, 104^{\circ}\text{E})]$, $[(15^{\circ}\text{N}, 108^{\circ}\text{E}), (15^{\circ}\text{N}, 102^{\circ}\text{E})]$ and $[(15^{\circ}\text{N}, 125^{\circ}\text{E}), (8^{\circ}\text{N}, 130^{\circ}\text{E})]$, respectively, which are on the three major water vapor transportation pathways to the key area: the southwesterly wind, the westerly wind, and the southeasterly wind. L is a constant (1800 km) in RH-SW, RH-W and RH-E. The RH values within the ellipse are modified as

$$\text{RH}_{\text{new}} = \text{RH}[(D - D_{12})/(L - D_{12})], \quad (2)$$

where D is the sum of distances from each grid point in do-

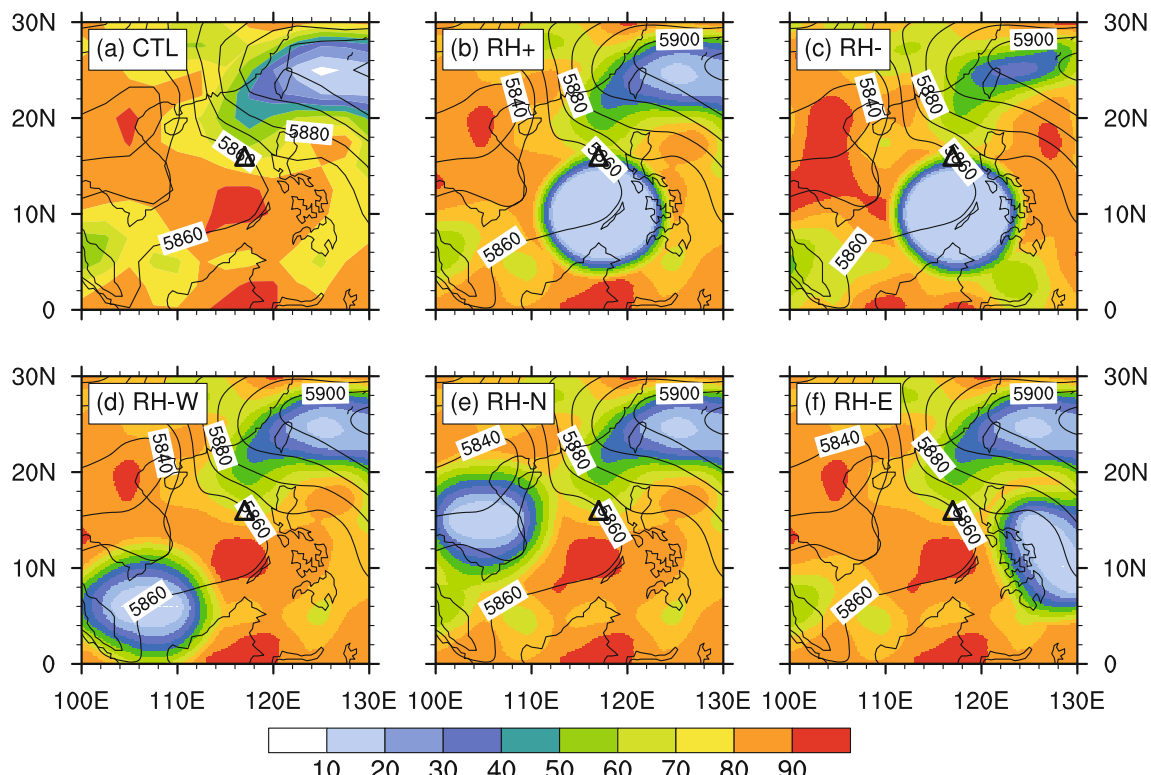


Fig. 2. The 500-hPa RH (color-shaded; units: %) in (a) CTL (NCEP), (b) RH-M, (d) RH-SW, (e) RH-W and (f) RH-S, and (c) the 400-hPa RH in RH-H at 0000 UTC 28 June 2001. Contours: 500-hPa geopotential height (units: gpm). The triangle denotes Durian's genesis location.

main 1 or 2 to the two focal points, and D_{12} is the distance between the two focal points. In RH-M and RH-H, L is varied, which is three times D_{12} . In order to clarify the effects of mid- and upper-level humidity in the key area on TC genesis and make the results of the sensitivity experiments more distinct, the RH values within the ellipse in RH-M and RH-H experiments were modified as

$$\text{RH}_{\text{new}} = \begin{cases} 0, & D_{12} < D < 2D_{12} \\ \text{RH}[(D - 2D_{12})/(L - 2D_{12})], & 2D_{12} < D < L \end{cases}, \quad (3)$$

in which the focal points of RH-M and RH-H were both located at $[(10^\circ\text{N}, 115^\circ\text{E}), (10^\circ\text{N}, 120^\circ\text{E})]$. All the sensitivity experiments were conducted using the same model and configuration as the CTL experiment, except the initial RH. As reported in the following sections, Durian (2001)'s genesis process was evaluated by using the simulation data of the third domain (6-km grid spacing) in the aforementioned six numerical experiments from 1200 UTC 28 June to 1200 UTC 1 July 2001, identified as $t = 12$ to 84 hours hereafter.

4. Results

4.1. Vortex formations in the CTL and sensitivity experiments

The CTL experiment reproduced the large-scale circulation background well (Fig. 3), including the position and intensity of the subtropical high and the trough in the westerly wind in the north, albeit the simulated subtropical high was a little stronger than observed. The simulation also presented the upper-level westerly and easterly jets, as well as three low-level jets around the monsoon trough: the westerly wind across over the Indo-China Peninsula, the southwesterly wind over the SCS, and the southeasterly wind at the southern edge of the subtropical high. The simulated Durian formed at about $t = 32$ h (0800 UTC 29 June 2001), about two hours later than observed, when a low-pressure center and a closed cyclonic circulation both appeared near the surface [Wang et al. (2016b, Figs. 1b–d and Fig. 2)].

Compared with the observed six-hourly track and intensity, CTL basically reproduced Durian (2001)'s moving track and development successfully (Fig. 4). Figure 4b presents the hourly evolution of minimum sea level pressure (MSLP) in the CTL and five sensitivity experiments. The MSLP in CTL remained nearly constant for about 20 hours and then started to decrease, corresponding with the genesis time of the near-surface vortex. Of interest were the MSLPs in the three sensitivity experiments: RH-SW, RH-W and RH-E. The formation times of TC vortices were similar to that in CTL, indicating that the initial surrounding dry air outside the key area had little impact on the genesis time. However, after about $t = 48$ h, the TC vortex in RH-W showed a lower intensification rate, while those in RH-SW and RH-E intensified faster than that in CTL. The initial mid-level dry air in the key area (RH-M) delayed the genesis of the TC vortex for 34 hours, which was not surprising. Rappin et al. (2010) pointed out that the mid-level saturation deficit appears to cause mid-

level convective downdraughts and lead to a longer incubation period for convection to moisten the middle troposphere, further postponing TC formation. The TC vortex eventually generated at $t = 66$ h in RH-M, which was very weak and developed rather slowly. Due to the impact of upper-level dry air (RH-H), the TC vortex did not form until $t = 52$ h, about 20 hours later than that in CTL, but developed faster than RH-M. The above results show that different distributions of the initial RH fields exerted different impacts on the TC genesis or subsequent development. The evolution of RH fields in the six experiments will be discussed in the next section.

4.2. Characteristics of RH distributions

Time-height cross sections of the RH field averaged in a 200-km-radius domain moving with the vortex circulation center are presented in Fig. 5. The mid-level vortex centers before TC formation and the TC centers after formation were selected as the circulation centers. Since the 200-km-radius area moved out of the third domain after $t = 64$ h, only the evolutions from $t = 12$ to 64 are presented. Figure 5 shows that the RH below $z = 7$ km in CTL exceeded 85% in the initial 36 hours, and then the RH between $z = 3$ and 9 km decreased slightly (Fig. 5a). The horizontal RH distribution at $z = 5$ km in CTL (Fig. 6a1) showed that an elongated mid-level vortex emerged within the high RH region ($>80\%$) at $t = 20$ h. With the expansion of the high RH region, the vortex became more axisymmetric at $t = 36$ h (not shown). However, possibly influenced by the establishment of the TC eye area and the dry air from the northeast at around $t = 42$ to 54 h, the RH near the circulation center and in the northeast phase of the vortex decreased (Figs. 6a2 and a3), corresponding to the RH reduction in Fig. 5a.

The RH above $z = 3$ km in RH-M and RH-H were significantly low in the first six hours (Figs. 5b and c), because of the reduction in mid- and upper-level RH in their initial conditions. However, the RH at $z = 4$ to 8 km in RH-H recovered to 85% more rapidly than that in RH-M. The mid-level dry air in the key area in RH-M stretched, while the moist westerly flow continued to humidify the west periphery of the dry-air belt (Figs. 6b1–b3). Eventually, a mid-level vortex formed in the high RH region at $t = 48$ h. Unlike the dry belt in RH-M, the mid-level high RH regions were sporadic at the beginning and then enhanced by the moist westerly and southeasterly flow (Figs. 6c1 and c2). The mid-level vortex did not form until $t = 48$ h in RH-H.

The RH constantly remained above 85% below $z = 7$ km in RH-SW and RH-E (Figs. 5d and f). The initial dry air to the southwest and to the east of the key area generally stayed away from the vortices rather than intruding into the inner cores (Figs. 6d1–d3 and 6f1–f3). Besides, the RH in RH-SW and RH-E distributed more symmetrically around the vortex centers than that in CTL. Backward trajectory analysis of mid-level parcels in the 200-km-radius area at $t = 60$ h in RH-SW was conducted using the Air Resources Laboratory's Hybrid Single-Particle Lagrangian Integrated Trajectory model (Stein et al., 2015; Rolph et al., 2017). Results showed that the potential moisture source region excluded the moisture

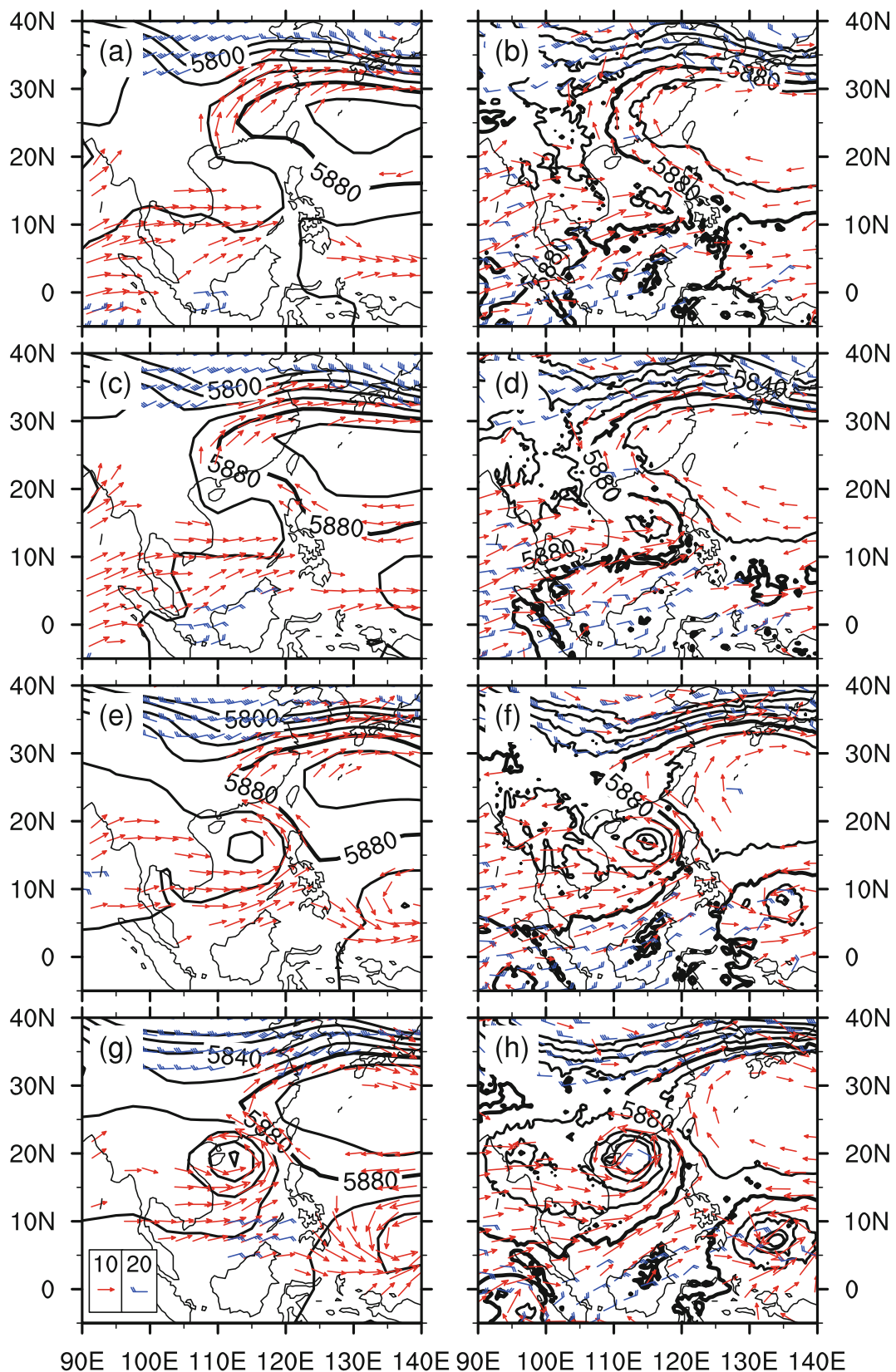


Fig. 3. The 500-hPa geopotential height (contours; units: gpm), 850-hPa wind field (red vectors; $>10 \text{ m s}^{-1}$; units: m s^{-1}) and 250-hPa wind field (blue wind bars; $>20 \text{ m s}^{-1}$; units: m s^{-1}) from (a, c, e, g) NCEP analysis data on a $2.5^\circ \times 2.5^\circ$ grid, and (b, d, f, h) numerical simulation data with grid spacing of 54 km (domain 1) at (a, b) $t = 18 \text{ h}$, (c, d) $t = 24 \text{ h}$, (e, f) $t = 48 \text{ h}$ and (g, h) $t = 72 \text{ h}$.

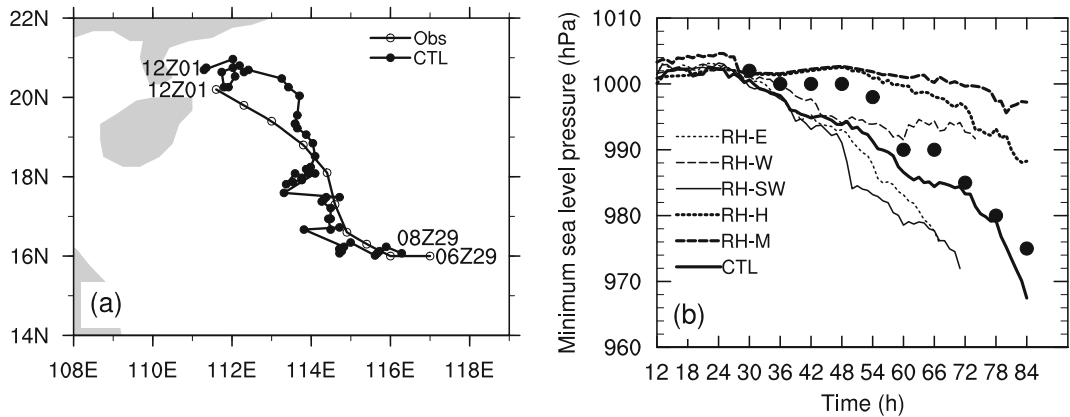


Fig. 4. (a) Storm tracks from observation (six-hourly) and CTL (hourly). (b) Temporal evolution of MSLP in the six experiments (lines) and observation (black dots). The vortex center in RH-E, RH-W and RH-SW moved out of the domain in the late stage of the simulation.

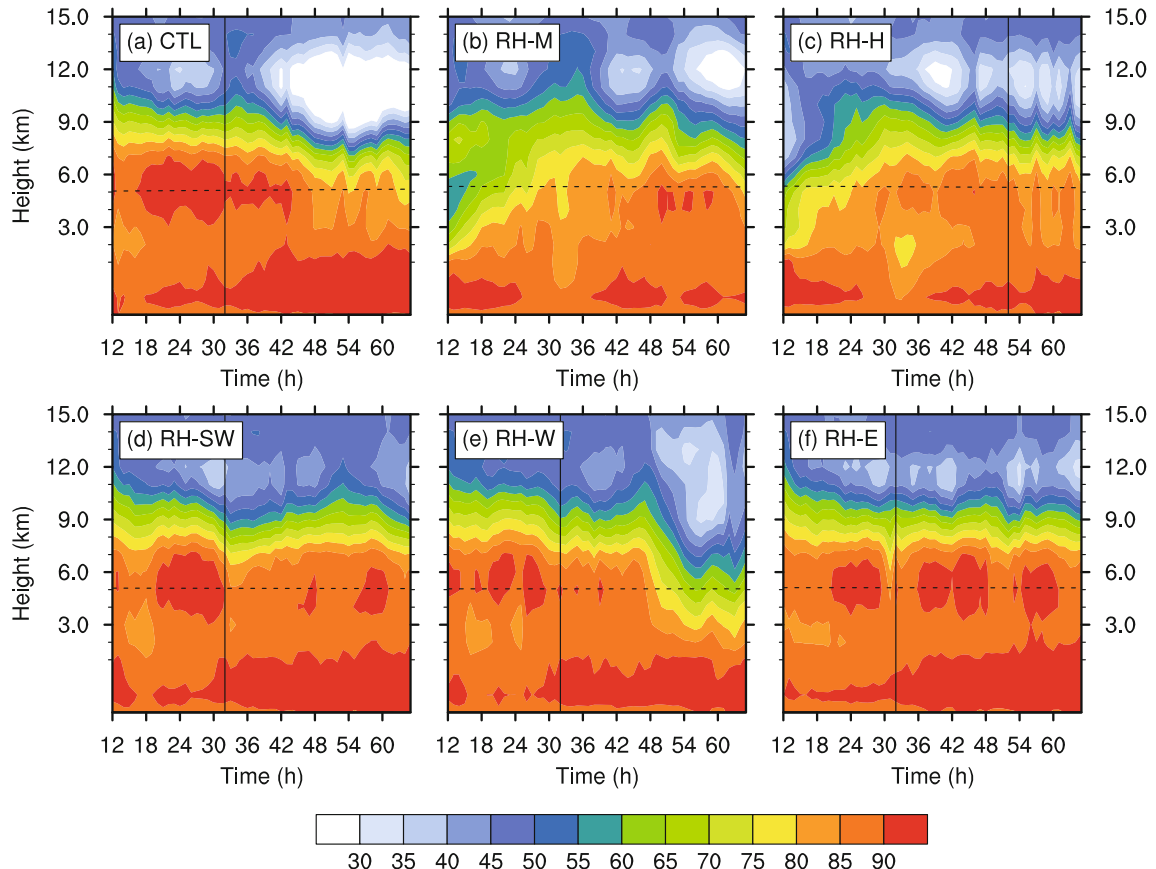


Fig. 5. Time–height cross sections of RH averaged within a radius of 200 km from the circulation center from $t = 12$ – 64 h in the six experiments. The vertical line denotes the formation time of the TC vortex, and the horizontal dashed line denotes 0°C altitude.

above the 800-hPa level (Fig. 7a), suggesting that the initial mid-level dry air in the southwest of the key area made little impact. Similar to RH-SW and RH-E, the dry air to the west of the key area (RH-W) also stayed away from the inner core (Figs. 6e1–e3). Although the dry air was still unable to intrude into the inner vortex, the high RH region in the

southwest periphery was reduced by eastward dry flow and southward moist flow (Figs. 6e1 and e2). Then, the RH in RH-W from $z = 4$ to 9 km significantly reduced after $t = 48$ h (Fig. 5e). Even so, a weak TC still developed. An analogous phenomenon was found by Braun et al. (2012): if dry air is only partially entrained and does not reach the center, devel-

opment may still occur, albeit the intensification rate may be reduced. Backward trajectory analysis in RH-W showed that there were a few trajectories that originated from the Indo-China Peninsula between 700 and 450 hPa (Fig. 7b), indicating that the initial mid-level dry air in RH-W might have influenced a fraction of the northeast phase of TC circulation at $t = 60$ h. Dunkerton et al. (2009) suggested that the kinematic–dynamic barrier or pouch containing the incipient TC provide a laterally permeable barrier to prevent the dry air from intruding into the TC inner core. In this study, we speculate that the dynamics and kinematics of the initial disturbance and the incipient TC might change due to the modification of RH, resulting in stronger pouches in RH-SW and RH-E, in which high RH sustained, and vulnerable pouches in RH-W and CTL. Freismuth et al. (2016) found that a compromised pouch may allow intrusion of dry air and hinder TC intensification. Besides, since the pattern of southwest/west flow encountering east flow (the left column of Fig. 6) still existed over the SCS and a low-level vortex eventually formed in every experiment, one can infer that the modification of

RH did not eliminate the typical structure of the monsoon trough, which was critical for TC formation. Thus, the different results among experiments were mainly associated with the moisture changes.

4.3. Water vapor budget analysis

The foregoing analysis implies that the distribution and variation of the RH field could impact TC formation and its subsequent intensification. Of interest was that, although dry air existed outside the key area in the initial conditions, the TCs in RH-SW and RW-E still intensified faster than that in CTL. This phenomenon could have been due to the decrease in RH at $z = 5$ to 9 km after $t = 42$ h in CTL but sustained near-saturated inner-core environments in RH-SW and RW-E. Different from RH-SW and RH-E, the vortex in RH-W, with the initial dry air to the west of the key area, eventually developed more slowly, caused by the RH reduction after TC formation as well. The other two sensitivity experiments showed that initial mid-level (RH-M) or upper-level (RH-H) dry air in the key area could significantly slow down the formation

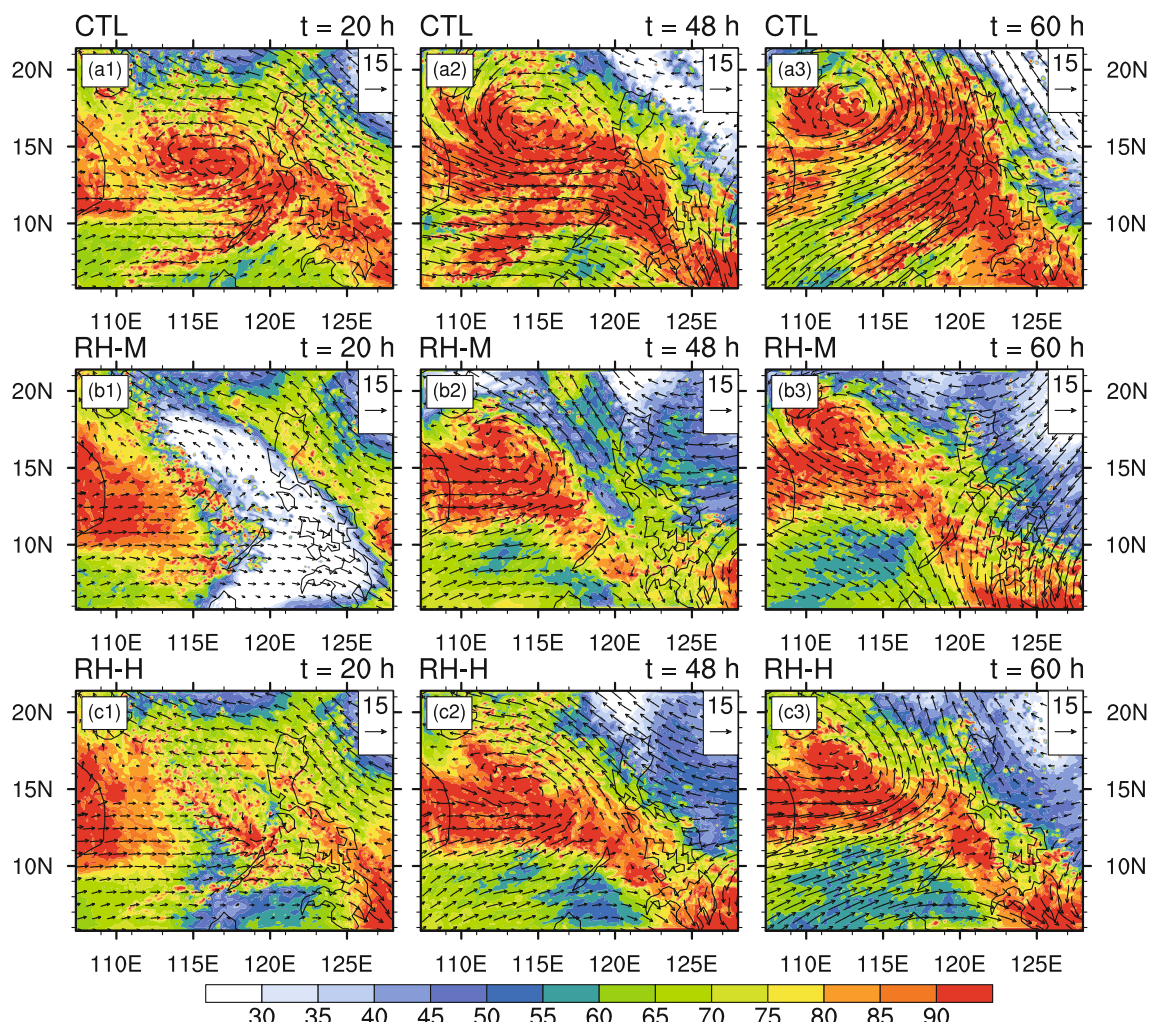


Fig. 6. Distribution of RH (color-shaded; units: %) and wind vectors (units: m s^{-1}) relative to the moving velocity of the averaging area at $z = 5$ km at $t = 20$ h, $t = 48$ h and $t = 60$ h for (a1–a3) CTL, (b1–b3) RH-M, (c1–c3) RH-H, (d1–d3) RH-SW, (e1–e3) RH-W, and (f1–f3) RH-E.

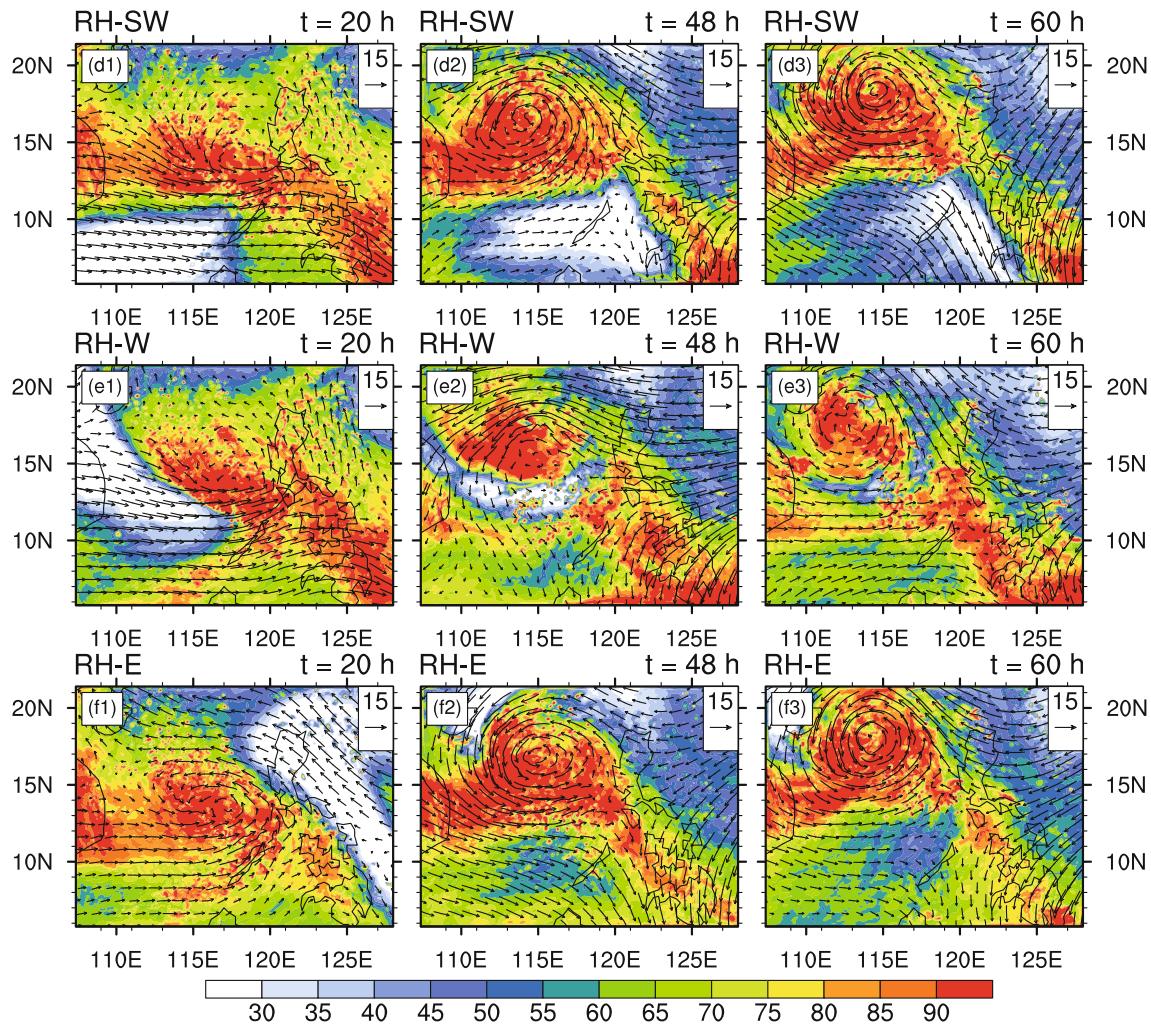


Fig. 6. (Continued)

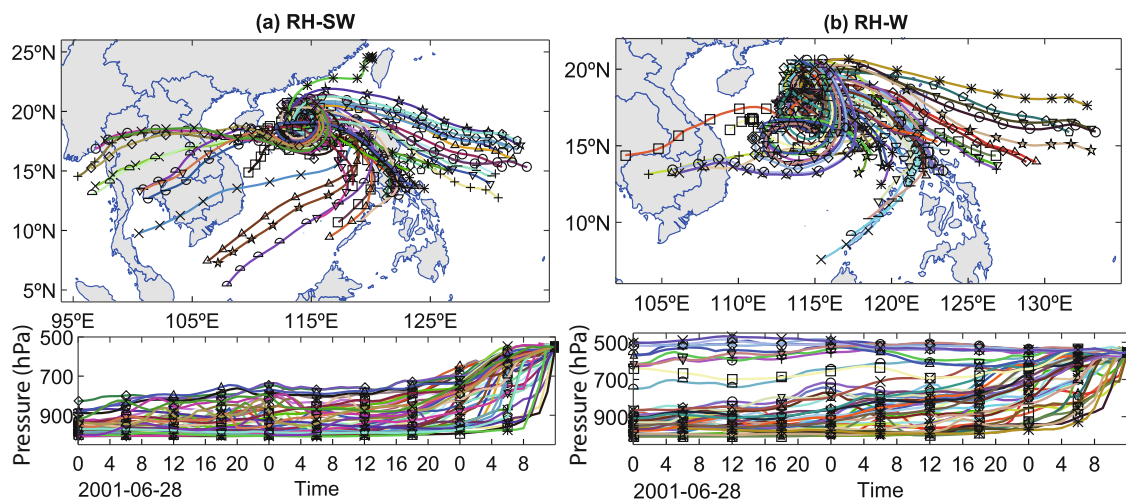


Fig. 7. The 60-hour (from 0000 UTC 28 June to 1200 UTC 30 June 2001) backward trajectories (upper) and trajectory height (bottom) of parcels at 5-km height in the 200-km-radius area centered on the TC center at $t = 60$ h (1200 UTC 30 June 2001) in (a) RH-SW and (b) RH-W using the HYSPLIT model. Trajectories are denoted by lines with different colors and markers. The input data are the simulation data with 54-km grid spacing from the WRF model (54 km).

of the TC vortex, especially in RH-M. Although it took several hours for the mid-level humidity to recover, a mid-level vortex and TC eventually formed in the high-humidity area in RH-M and RH-H. In summary, the mid-level humidity may not only affect the occurrence of the mid-level vortex and TC vortex during TC formation (Nolan, 2007), but also influence further development of the TC after its formation. In this section, water vapor budgets were examined to further investigate how the recovery of mid-level water vapor in RH-M and RH-H occurred, and how the mid-level moisture preserved after TC formation in RH-SW and RH-E, but decreased in CTL and RH-W.

Water vapor budget analysis has been used in previous studies (Fritz and Wang, 2013, 2014). The water budget equation in cylindrical coordinates is as follows, according to Fritz and Wang (2014):

$$\frac{\partial q_v}{\partial t} = -\frac{1}{r} \left[\frac{\partial(rq_v u)}{\partial r} + \frac{\partial(q_v v)}{\partial \lambda} \right] - \frac{\partial(q_v w)}{\partial z} + q_v \left[\frac{1}{r} \frac{\partial(ru)}{\partial r} + \frac{1}{r} \frac{\partial v}{\partial \lambda} + \frac{\partial w}{\partial z} \right] - NC + B_v + R, \quad (4)$$

where q_v is the water vapor mixing ratio; u and v are the storm-relative radial and tangential winds; w is the vertical velocity; r is the radius with respect to the circulation center;

the term on the left-hand side of Eq. (4) is the water vapor tendency (WVT); the first two terms on the right-hand side (RHS) are the horizontal flux convergence (HFC) term, and the vertical flux convergence (VFC) term, respectively; the third term on the RHS is the divergence (DIV) term; NC is the net condensation; and B_v represents the contributions from the planetary boundary layer parameterization to the water vapor budget. Except terms HFC and VFC, terms WVT, NC and B_v are directly output from the model. R represents the residual term, including the numerical modeling and calculation errors, the effects of turbulent mixing and diffusion.

Figure 8 shows the time series of the water vapor budget terms after vertically mass integrating from $z = 3$ to 9 km, and area averaging in a 200-km-radius domain moving with the vortex circulation center during the period $t = 12$ to 60 h. Although Fig. 8 shows that the WVT had strong fluctuations, the water vapor gains before $t = 30$ h were obvious in RH-M and RH-H (Figs. 8b and c), corresponding with the significantly increasing RH in Figs. 5b and c. Terms HFC, VFC, DIV and NC were the dominant terms, while B_v made little contribution. In the first 10 hours in RH-M and RH-H, the moistening was mainly contributed by VFC and DIV, offset by HFC and NC. Then, HFC generally became positive or weakly negative. Such variation was consistent with the results in Fritz and Wang (2014), in which the radial mois-

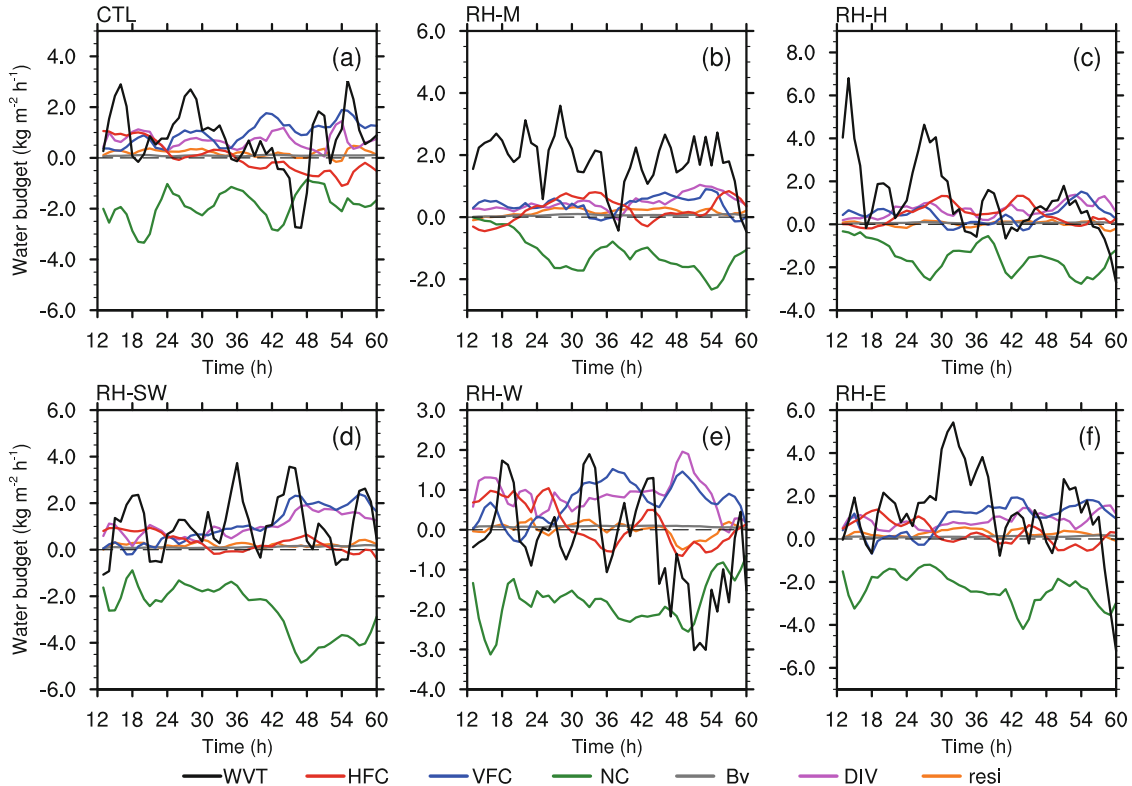


Fig. 8. Time series of three-hour running averaged water vapor budget terms, vertically mass integrated at mid-to-upper levels ($z = 3$ –9 km) and area-averaged within a radius of 200 km from the circulation center during $t = 12$ –64 h in the six experiments: (a) CTL; (b) RH-M; (c) RH-H; (d) RH-SW; (e) RH-W; (f) RH-E. WVT: net water vapor tendency; HFC: horizontal flux convergence; VFC: vertical flux convergence, NC: net condensation; B_v : contributions from the planetary boundary layer parameterization; DIV: divergence; resi: residual. Units: $\text{kg m}^{-2} \text{h}^{-1}$ for all terms except WVT, whose units are $10^{-1} \text{ kg m}^{-2} \text{h}^{-1}$. The horizontal dashed line denotes 0.

ture flux above 850 hPa increased significantly after genesis, probably caused by the deeper inflow layer associated with the establishment of the secondary circulation during TC genesis. Meanwhile, the VFC and NC terms slightly increased as TC formation approached.

Consistent with the foregoing analyses, obvious mid- and upper-level drying at $z = 3$ to 9 km occurred during $t = 42$ to 50 h in CTL and during $t = 45$ to 58 h in RH-W (Figs. 8a and e). Terms VFC and DIV were still the major sources, while NC was the major sink of water vapor. HFC was also a weak water vapor source before the drying happened. During the periods of air drying in these two experiments, HFC became negative while VFC and DIV exhibited slight reductions. The negative effect of HFC, together with the water vapor loss associated with the NC term, could not be compensated by VFC and DIV, leading to air drying. Fritz and Wang (2014) suggested that the vertically integrated inward moisture flux (HFC) accounts for a majority of the total condensation in the air column, whereas our study suggested that the vertical moisture flux (VFC) and DIV, instead of the HFC, were the major contributors to mid-level humidity. In RH-SW and RH-E (Figs. 8d and f), although the WVTs still oscillated around 0.0 intermittently, positive tendencies were obvious, to which HFC made a positive or very weak negative contribution. Besides, the VFC and NC terms showed distinct increasing trends, indicating continuous vertical transportation of water vapor and cloud development during TC genesis and sequential intensification.

In summary, the VFC term and DIV term were the two major sources of moisture at $z = 3$ –9 km, while the NC was the major sink in all experiments. Of interest was the HFC term, which basically made a positive contribution or weak negative contribution in mid-level air moistening processes. In air drying processes, it made an obvious negative contribution. Generally, a deep-depth of moisture in the troposphere is necessary for TC formation. A near-saturated environment is favorable for the development of deep convection and TC spin-up. Wang et al. (2010) and Wang (2012) suggested that the development of the secondary circulation during TC genesis is determined by both convective and stratiform processes. Thus, the different TC intensification rates in different experiments will be interpreted from the perspective of convective and stratiform processes. Their responses to moisture change and their contributions to TC intensification will be discussed in the following section.

5. Stratiform versus convective precipitation

5.1. Partitioning of stratiform and convective precipitation

The partitioning of precipitation/cloud into convective and stratiform type follows the methods used in Tao et al. (1993), Braun et al. (2010) and Wang et al. (2010). First, model grid points with surface rainfall rates greater than 25 mm h^{-1} were classified as convective. Second, if the surface rainfall rate of a grid point was twice as large as the aver-

age of its nearest four neighbors, the grid point, as well as its nearest four grids, were also categorized as convective. Convective columns, in which significant precipitation has not yet reached the surface, but with maximum vertical upward motions greater than 5 m s^{-1} , or cloud liquid water contents below the melting level larger than 0.5 g kg^{-1} , were also treated as convective. Precipitation in all remaining grids was considered to be stratiform.

The partitioning results showed that convective precipitation accounted for about 20%–50% of the area in the 100-km-radius circular domain moving with the circulation center (Fig. 9), distributed in both the TC circulation and the MCSs with higher rain rates (not shown). Stratiform precipitation, with a lower rain rate, covered a maximum of 80% of the area in CTL, RH-SW, RH-W and RH-E, and was above 60% in the other two experiments. Figure 9 also shows that the areal fraction of convection fluctuated and generally had a clear increasing trend during TC formation, as well as the following intensification, except that in RH-H. The relatively high fraction of convection in RH-H before $t = 32$ h (Fig. 9c) was probably owing to the convection in the mature MCSs before TC genesis. The fraction of stratiform precipitation remained constant or exhibited a slight decreasing trend in CTL, RH-SW, RH-W and RH-E (Figs. 9a, d, e and f), while those in RH-M and RH-H showed slight increasing trends (Figs. 9b and c) as the air column approached moist-saturation. It can also be seen that both convective and stratiform precipitation were inhibited by a drier environment. The valleys of areal fraction values in CTL (at $t = \sim 48$ h), RH-W ($t = \sim 48$ –54 h), RH-M (before $t = \sim 24$ h) and RH-H (before $t = \sim 24$ h and at $t = \sim 36$ h) corresponded well to the lower RH periods in Fig. 5.

5.2. Roles of convective and stratiform precipitation in TC development

Figure 10 presents the vertical mass flux and the diabatic heating rate associated with the convective and stratiform precipitation. The diabatic heating rate was calculated by the residual of the potential temperature field (θ) in space and time (Hendricks et al., 2004); that is, $\dot{\theta} = \partial\theta/\partial t + \mathbf{v} \cdot \nabla\theta$, where \mathbf{v} is the three-dimensional velocity vector. Figure 10 shows that the convective cloud generally produced upward mass flux through the whole troposphere, while the stratiform cloud produced downward mass flux below 6 km and upward mass flux above that altitude. The diabatic heating usually corresponded to upward mass flux, while cooling corresponded to downward mass flux. Coincident with the mid-to-upper-layer dry-air intrusion in CTL during $t = 42$ to 50 h, and in RH-W during $t = 45$ to 58 h, the mass flux associated with convection above 4 km became weaker (Figs. 10a and e), due to the inhibitory effect of dry air on deep convection. Consequently, the diabatic heating rate was reduced remarkably. In the following air moistening, the mass flux associated with convection rapidly recovered again. The initial dry-air patches in RH-M and RH-H also significantly suppressed the upward mass flux during the first 10 hours (Figs. 10b and c). Although the air was gradually moistened thereafter,

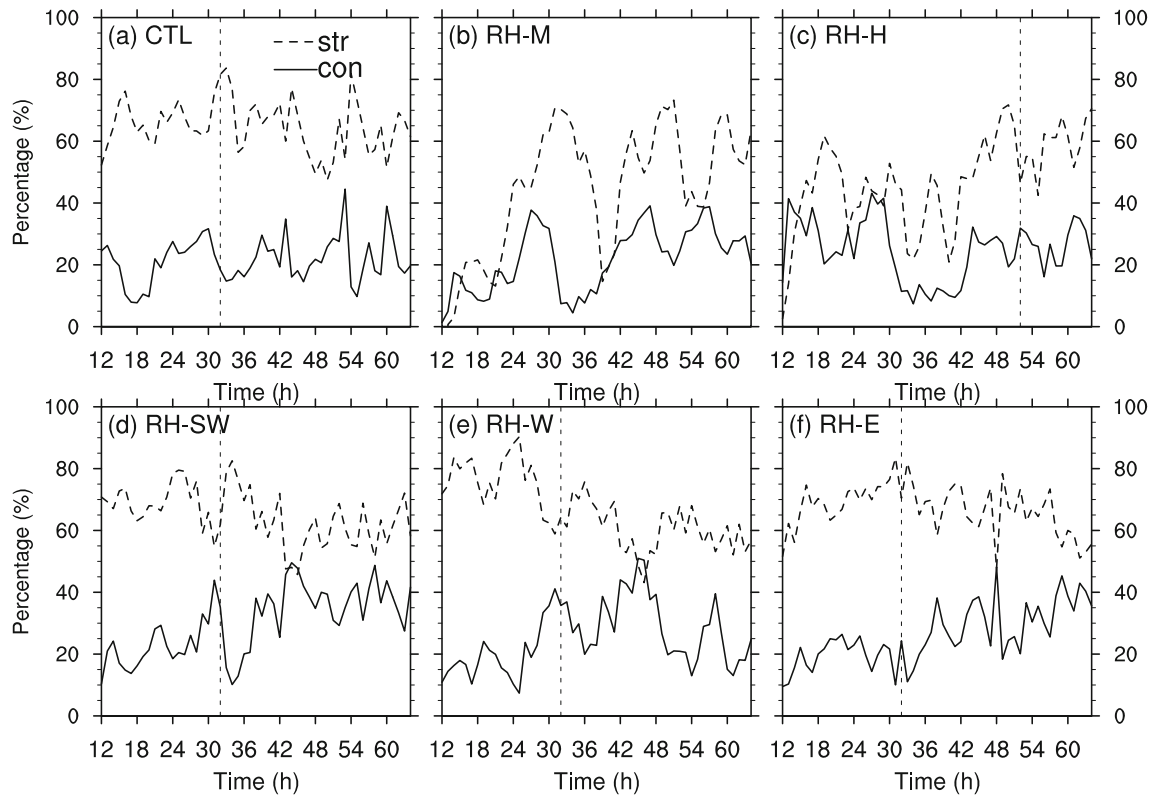


Fig. 9. Convective and stratiform areal coverage percentage (%) according to the total number of pixels within a radius of 100 km in (a) CTL, (b) RH-M, (c) RH-H, (d) RH-SW, (e) RH-W and (f) RH-E, from $t = 12$ –64 h. Dashed lines: stratiform precipitation; solid lines: convective precipitation. The vertical line denotes the formation time of the TC vortex.

the intensity of mass flux in these two experiments was still weaker compared with that in CTL. Besides, the weaker convection near the surface layers in RH-M and RH-H was associated with relatively shallow near-saturated air there compared with CTL (Figs. 5a–c). The constantly upward mass flux in RH-SW and RH-E was not only stronger than others, but also expanded to a deeper layer.

The response of the stratiform process to air drying was more obvious. The upward mass flux and diabatic heating rate between 6–12 km were largely reduced and even became downward mass flux and diabatic cooling after $t = \sim 42$ h in CTL and after $t = \sim 48$ h in RH-W (Figs. 10g and k). Meanwhile, the cooling and downward mass flux below 6 km became weaker, owing to less condensate melting and evaporation. Similarly, the initial dryer environment in RH-M and RH-H suppressed the stratiform process, by converting upper-layer upward mass flux to downward and reducing the intensity of lower-layer downward mass flux. Previous studies (James and Markowski, 2010; Smith and Montgomery, 2012; Kilroy and Smith, 2013) have suggested that dry air is detrimental to moist convection by mainly inhibiting the intensity of updrafts and upward mass flux. In this work, the suggestion is that the mid- and upper-layer dry air is detrimental to both the convective and stratiform process, by mainly inhibiting their upward mass flux above the lower troposphere. In turn, weak mid-level upward mass flux in-

duced weak horizontal convergence and vertical transportation, which made very weak and slow air moistening (Fig. 8). The dry air also suppressed the intensity of the stratiform process by reducing downdrafts at lower-tropospheric layers. Even so, because the magnitudes of mass flux and diabatic heating rate associated with stratiform precipitation were much smaller than those associated with convection, the downward mass flux or cooling above 6 km associated with stratiform cloud were generally offset by upward mass flux and heating associated with convection. Thus, convection still played a dominant role in upward mass transportation and heating, which are essential to the development of secondary circulation during TC formation and intensification.

5.3. Vorticity budget analysis

Since the vortex spin-up during TC genesis and intensification is closely related to vorticity amplification, the vorticity budget was diagnosed to further understand the different intensification rates in the six experiments. The vorticity budget equation in the expression of temporal change of the circulation C in Davis and Galarneau (2009) is adopted in this paper:

$$\frac{\partial C}{\partial t} = - \oint \eta \mathbf{V} \cdot \hat{\mathbf{n}} dl + \oint \omega \left(\hat{\mathbf{k}} \times \frac{\partial \mathbf{V}}{\partial p} \right) \cdot \hat{\mathbf{n}} dl + \oint (\hat{\mathbf{k}} \times \mathbf{F}) \cdot \hat{\mathbf{n}} dl, \quad (5)$$

Convergence Tilting Friction

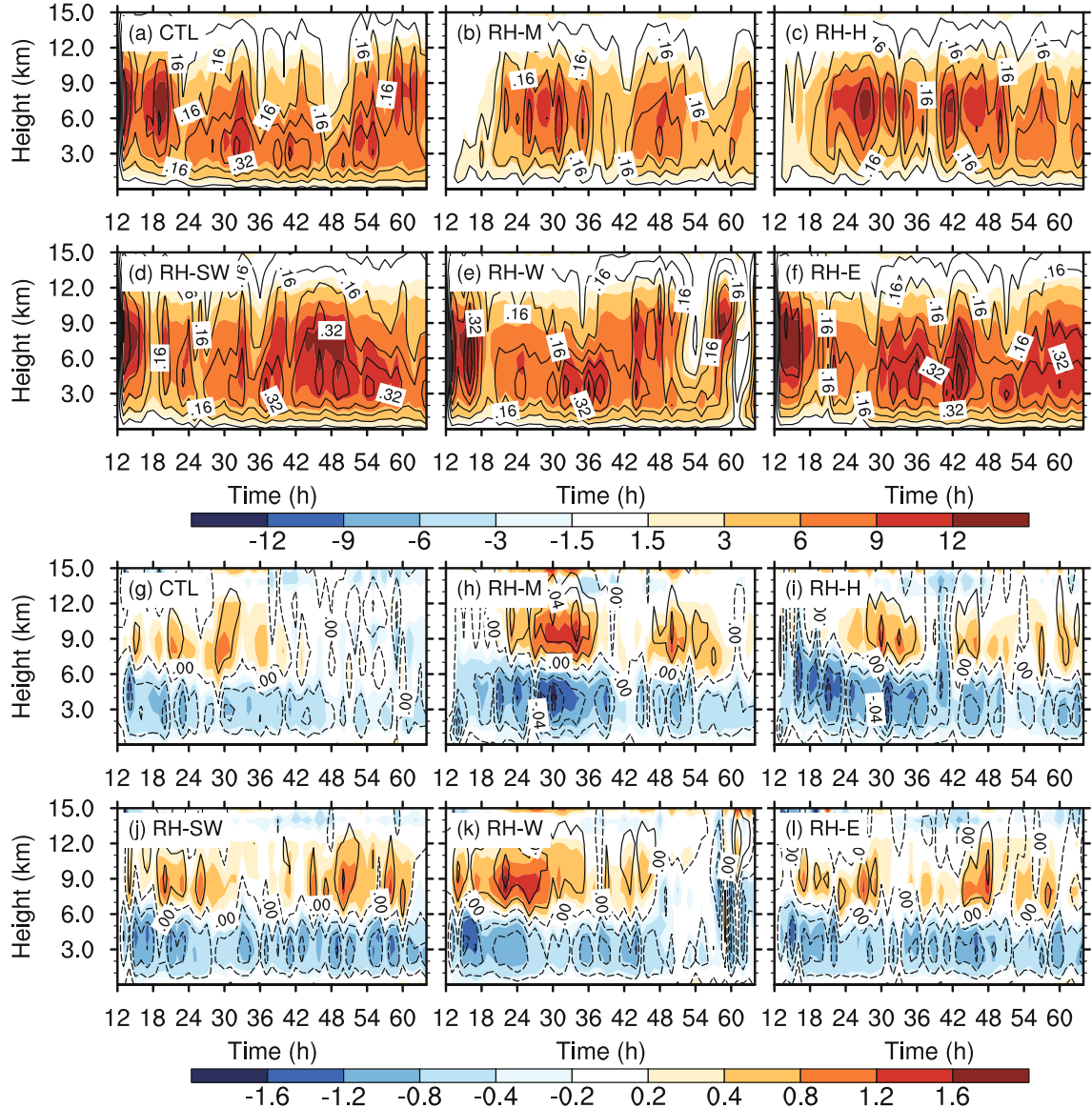


Fig. 10. Time–height cross sections of mass flux (contours; units: $\text{kg m}^{-2} \text{s}^{-1}$) and diabatic heating rate (color-shaded; units: K h^{-1}) associated with (a–f) convective and (g–l) stratiform cloud, averaged within a radius of 200 km from the circulation center, from $t = 12\text{--}64$ h, in the six experiments: (a, g) CTL; (b, h) RH-M; (c, i) RH-H; (d, j) RH-SW; (e, k) RH-W; (f, l) RH-E.

where η is the absolute vertical vorticity, \mathbf{V} is the storm-relative horizontal wind vector, ω is the vertical velocity on isobaric coordinates, $\hat{\mathbf{k}}$ is the unit vector in the vertical direction, and \mathbf{F} is the friction vector. Equation (5) contains closed line integrals evaluated around a square box; thus, $\hat{\mathbf{n}}$ is the unit vector normal to the edges of the box and dl is the differential along the perimeter of the box. The contribution to the local change in circulation is separated into three terms on the RHS of Eq. (5): the convergence of the horizontal advective flux of vertical vorticity, the tilting term, and the friction term, respectively. The friction term, which includes numerical dissipation and boundary layer effects, is neglected here. The terms in Eq. (5) are divided by the boxed area in the following analysis.

Figure 11 shows the vertical profiles of vorticity tendency, the convergence term, and the tilting term area, temporally averaged in a 400×400 km box in three periods of the six experiments: $t = 12\text{--}24$ h, $t = 27\text{--}39$ h, and $t = 42\text{--}54$ h. The results were computed based on 10-min model output data. It can be seen that, generally, the convergence of vorticity flux was the major source of low-to-middle-level vorticity amplification, while the convergence term above mid-levels made a negative contribution. The tilting term in the lower levels had a small negative effect on vorticity tendency, while that at mid- and upper-levels became the major source. In CTL, cyclonic vorticity grew in the low-to-mid troposphere before $t = 39$ h (Figs. 11a1 and a2), which was analogous to those in RH-SW and RH-E in terms of magnitude and ver-

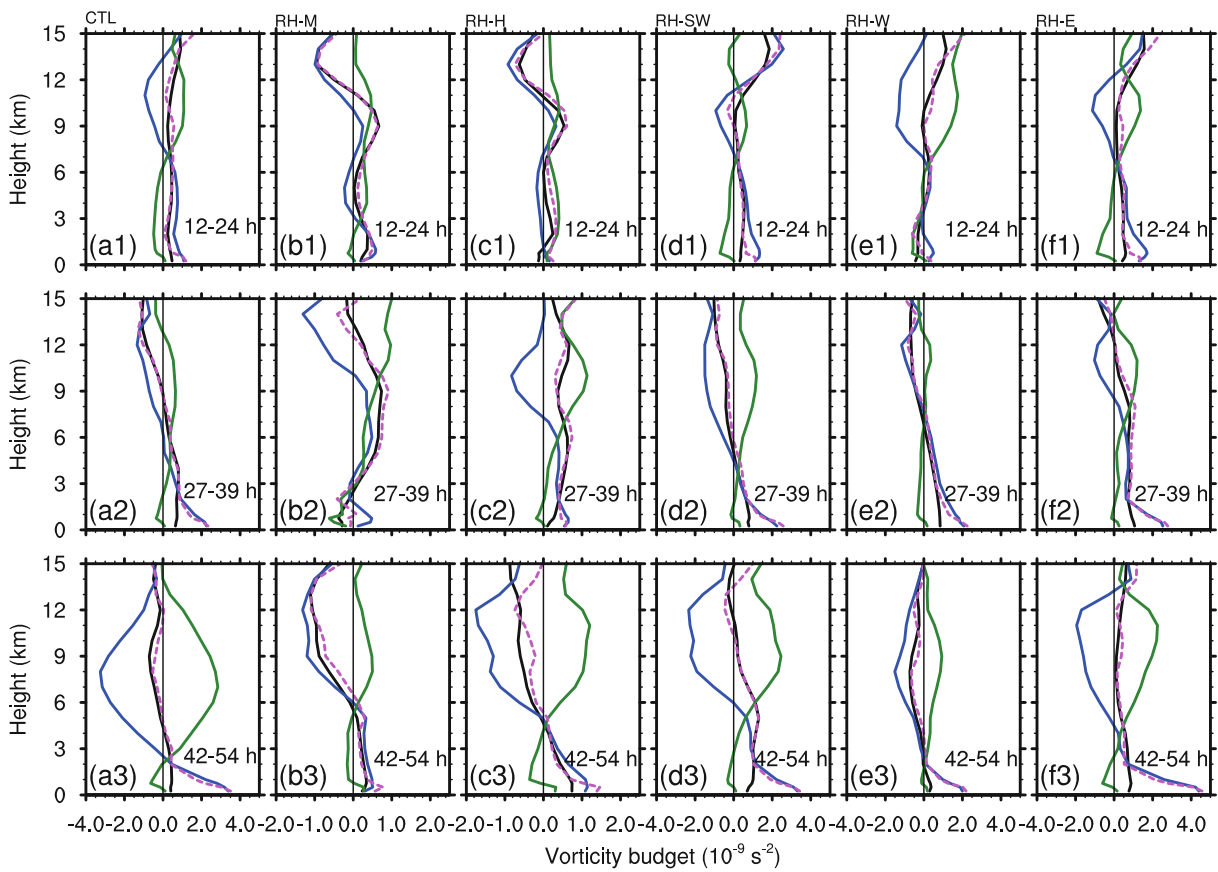


Fig. 11. Vertical profiles of vorticity budget terms temporally and area-averaged from (a1–f1) $t = 12\text{--}24 \text{ h}$, (a2–f2) $t = 27\text{--}39 \text{ h}$, and (a3–f3) $t = 42\text{--}54 \text{ h}$, within a 400-km-long box moving with the storm: vorticity tendency (black line), contributions to the total circulation tendency (magenta dash line) due to vorticity convergence (blue line), and vortex tilting (green line) of Eq. (5). Units: 10^{-9} s^{-2} . The vertical thin line denotes zero.

tical structure. The lower-tropospheric vorticity in RH-W first underwent a decline, during $t = 12\text{--}24 \text{ h}$, and then an increase during $t = 27\text{--}39 \text{ h}$ (Figs. 11e1 and e2). The significant amplifications of low-level vorticity during $t = 27\text{--}39 \text{ h}$ corresponded well to the spin-up timing of the low-level TC vortex in CTL, RH-SW, RH-W and RH-E. Unlike the continuous vorticity increasing through the deep troposphere in RH-SW and RH-E during $t = 42\text{--}54 \text{ h}$ (Figs. 11d3 and f3), the vorticity above the lower troposphere decreased in CTL and RH-W (Figs. 11a3 and e3). The negative vorticity tendency was owing to the negative contribution of the convergence term, which was partly offset by the positive effect of the tilting term. Generally, a positive convergence term is largely a result of stretching of the vortex vorticity by organized deep convection (Montgomery et al., 2006). Since deep convection and the associated upward mass flux were significantly inhibited by dryer air in CTL and RH-W after TC formation, according to the foregoing analysis (Figs. 10a and e), the convergence term above 2–3 km became negative, resulting in the decrease of mid- and upper-level vorticity. Thus, the vertical coherence and the rapid intensification was inhibited in CTL and RH-W.

As for RH-M and RH-H, the convergence terms during $t = 12\text{--}24 \text{ h}$ above the lower troposphere were weak and even

negative (Figs. 11b1 and c1), as the initial dryer environment inhibited the vertical development of convection (Figs. 10b and c). Owing to the relatively weak convection, the magnitudes of low-level vorticity tendency in RH-M and RH-H were still much smaller than those in other experiments (Figs. 11b2–b3 and c2–c3), resulting in slower TC formation and intensification.

6. Summary and conclusions

Both climatological statistics and synoptic analyses have shown that mid-level moisture plays an important role in TC genesis. In our study, the influence of mid- and upper-level low-saturation air (dry air) on TC genesis was investigated by conducting a series of sensitivity experiments on the formation process of TC Durian (2001). The initial RH field was reduced in different places relative to the genesis location of Durian (2001). Further, the sources and sinks of moisture were investigated and the relative contributions of different precipitation types to the TC formation and the following intensification were discussed.

A high RH (>90%) region in the central SCS in the control experiment (CTL) was denoted as the key area. Sensitivity experiments showed that, when mid-level (RH-M) or

upper-level (RH-H) dry air existed in the key area, the formation of the TC was delayed for 34 and 20 hours respectively, compared with CTL, and developed rather slowly. As Emanuel et al. (2008) and Rappin et al. (2010) pointed out, the mid-level saturation deficit would lead to a longer incubation period of TC formation, because it takes some time for convection to moisten the middle atmosphere and diminish the impact of convective downdrafts. The initial mid- or upper-level dry air in the central SCS eventually disappeared after being moistened in about 20 hours. The effects of initial dry air surrounding the key area were also examined. Results showed that dry air in the upstream southwest flow of the monsoon trough (RH-SW), in the upstream west flow of the monsoon trough (RH-W), and on the east of the monsoon trough (RH-E), had little influence on the formation time of the TC. Instead, the TC in RH-SW and RH-E intensified more quickly than that in CTL and RH-W. This phenomenon was accompanied by a decrease in RH at $z = 5\text{--}9\text{ km}$ after formation in CTL and RH-W and the sustained near-saturated environment in RH-SW and RW-E. In summary, the mid-level humidity would affect the occurrence of the incipient TC vortex and its further intensification. The rapid development of the TC was accompanied by sustained near-saturated mid- and upper-level air, whereas low humidity would decelerate the development. Besides, dry air around the key area was not able to intrude into the inner core of the TC vortex, but stay at the periphery, similar to the dry air entrainment in the case of tropical storm Fay (2008) in Fritz and Wang (2013).

The water vapor budget equation was applied to investigate the mid- and upper-level humidity change in all sensitivity experiments. Results showed that the vertical moisture flux convergence term and the moisture DIV term were the two major sources and the condensation term was the major sink. The mid- and upper-level air moistening or high humidity sustaining processes were accompanied by a positive contribution of horizontal moisture flux convergence, while the air drying processes were accompanied by negative horizontal flux convergence.

As the TC generated and intensified, convective cloud essentially kept on developing in terms of larger area coverage. However, the development of convective precipitation was interrupted by mid- and upper-level air drying, resulting in weaker upward mass flux and diabatic heating above the lower troposphere in CTL, RH-W, RH-M and RH-H. The stratiform clouds in these experiments were also inhibited, in which weak upward mass flux above 6 km became downward, and the associated diabatic heating became cooling. Overall, the contribution of convection to vertical mass flux and diabatic heating still dominated the TC developing process. The TC development rate in all experiments was closely related to the vorticity tendency. A negative vorticity tendency above the lower troposphere led to the slower intensification rate in CTL, RH-W, RH-M and RH-H. The negative effect of the convergence of vorticity flux term, which was closely related to inhibited convection above the lower troposphere, determined the decrease in vorticity during air drying or in a dryer environment.

Acknowledgements. Yaping WANG and Xiaopeng CUI are supported by the National Basic Research (973) Program of China (Grant No. 2015CB452804). Thanks also go to the NOAA Air Resources Laboratory for providing the HYSPLIT_4 model.

REFERENCES

- Bister, M., 2001: Effect of peripheral convection on tropical cyclone formation. *J. Atmos. Sci.*, **58**, 3463–3476, [https://doi.org/10.1175/1520-0469\(2001\)058<3463:EOPCOT>2.0.CO;2](https://doi.org/10.1175/1520-0469(2001)058<3463:EOPCOT>2.0.CO;2).
- Bister, M., and K. A. Emanuel, 1997: The genesis of Hurricane Guillermo: TEXMEX analyses and a modeling study. *Mon. Wea. Rev.*, **125**, 2662–2682, [https://doi.org/10.1175/1520-0493\(1997\)125<2662:TGOHGT>2.0.CO;2](https://doi.org/10.1175/1520-0493(1997)125<2662:TGOHGT>2.0.CO;2).
- Braun, S. A., 2010: Reevaluating the role of the Saharan air layer in Atlantic tropical cyclogenesis and evolution. *Mon. Wea. Rev.*, **138**, 2007–2037, <https://doi.org/10.1175/2009MWR3135.1>.
- Braun, S. A., M. T. Montgomery, K. J. Mallen, and P. D. Reasor, 2010: Simulation and interpretation of the genesis of tropical storm Gert (2005) as part of the NASA tropical cloud systems and processes experiment. *J. Atmos. Sci.*, **67**, 999–1025, <https://doi.org/10.1175/2009JAS3140.1>.
- Braun, S. A., J. A. Sippel, and D. S. Nolan, 2012: The impact of dry midlevel air on hurricane intensity in idealized simulations with no mean flow. *J. Atmos. Sci.*, **69**, 236–257, <https://doi.org/10.1175/JAS-D-10-05007.1>.
- Davis, C. A., and T. J. Galarneau Jr, 2009: The vertical structure of mesoscale convective vortices. *J. Atmos. Sci.*, **66**, 686–704, <https://doi.org/10.1175/2008JAS2819.1>.
- Davis, C. A., and D. A. Ahijevych, 2012: Mesoscale structural evolution of three tropical weather systems observed during PREDICT. *J. Atmos. Sci.*, **69**, 1284–1305, <https://doi.org/10.1175/JAS-D-11-0225.1>.
- Dunion, J. P., and C. S. Velden, 2004: The impact of the Saharan air layer on Atlantic tropical cyclone activity. *Bull. Amer. Meteor. Soc.*, **85**, 353–366, <https://doi.org/10.1175/BAMS-85-3-353>.
- Dunkerton, T. J., M. T. Montgomery, and Z. Wang, 2009: Tropical cyclogenesis in a tropical wave critical layer: Easterly waves. *Atmospheric Chemistry and Physics*, **9**, 5587–5646, <https://doi.org/10.5194/acp-9-5587-2009>.
- Emanuel, K. A., 1989: The finite-amplitude nature of tropical cyclogenesis. *J. Atmos. Sci.*, **46**, 3431–3456, [https://doi.org/10.1175/1520-0469\(1989\)046<3431:TFANOT>2.0.CO;2](https://doi.org/10.1175/1520-0469(1989)046<3431:TFANOT>2.0.CO;2).
- Emanuel, K., R. Sundararajan, and J. Williams, 2008: Hurricanes and global warming: Results from downscaling IPCC AR4 simulations. *Bull. Amer. Meteor. Soc.*, **89**, 347–368, <https://doi.org/10.1175/BAMS-89-3-347>.
- Emanuel, K., C. DesAutels, C. Holloway, and R. Korty, 2004: Environmental control of tropical cyclone intensity. *J. Atmos. Sci.*, **61**, 843–858, [https://doi.org/10.1175/1520-0469\(2004\)061<0843:ECOTCI>2.0.CO;2](https://doi.org/10.1175/1520-0469(2004)061<0843:ECOTCI>2.0.CO;2).
- Freismuth, T. M., B. Rutherford, M. A. Boothe, and M. T. Montgomery, 2016: Why did the storm ex-Gaston (2010) fail to redevelop during the PREDICT experiment? *Atmospheric Chemistry and Physics*, **16**, 8511–8519, <https://doi.org/10.5194/acp-16-8511-2016>.
- Fritz, C., and Z. Wang, 2013: A numerical study of the impacts of dry air on tropical cyclone formation: A development case and a nondevelopment case. *J. Atmos. Sci.*, **70**, 91–111, <https://doi.org/10.1175/JAS-D-12-018.1>.

- Fritz, C., and Z. Wang, 2014: Water vapor budget in a developing tropical cyclone and its implication for tropical cyclone formation. *J. Atmos. Sci.*, **71**, 4321–4332, <https://doi.org/10.1175/JAS-D-13-0378.1>.
- Fritz, C., Z. Wang, S. W. Nesbitt, and T. J. Dunkerton, 2016: Vertical structure and contribution of different types of precipitation during Atlantic tropical cyclone formation as revealed by TRMM PR. *Geophys. Res. Lett.*, **43**, 894–901, <https://doi.org/10.1002/2015GL067122>.
- Ge, X. Y., T. Li, and M. Peng, 2013: Effects of vertical shears and midlevel dry air on tropical cyclone developments. *J. Atmos. Sci.*, **70**, 3859–3875, <https://doi.org/10.1175/JAS-D-13-066.1>.
- Gray, W. M., 1968: Global view of the origin of tropical disturbances and storms. *Mon. Wea. Rev.*, **96**, 669–700, [https://doi.org/10.1175/1520-0493\(1968\)096<0669:GVOTOO>2.0.CO;2](https://doi.org/10.1175/1520-0493(1968)096<0669:GVOTOO>2.0.CO;2).
- Gray, W. M., 1977: Tropical cyclone genesis in the Western North Pacific. *J. Meteor. Soc. Japan*, **55**, 465–482.
- Gray, W. M., 1979: Hurricanes: Their formation, structure and likely role in the tropical circulation. *Meteorology over the Tropical Oceans*, D. B. Shaw, Ed., James Glaisher House, 155–218.
- Hendricks, E. A., M. T. Montgomery, and C. A. Davis, 2004: The role of “vortical” hot towers in the formation of Tropical Cyclone Diana (1984). *J. Atmos. Sci.*, **61**, 1209–1232, [https://doi.org/10.1175/1520-0469\(2004\)061<1209:TROVHT>2.0.CO;2](https://doi.org/10.1175/1520-0469(2004)061<1209:TROVHT>2.0.CO;2).
- Hong, S. Y., Y. Noh, and J. Dudhia, 2006: A new vertical diffusion package with an explicit treatment of entrainment processes. *Mon. Wea. Rev.*, **134**, 2318–2341, <https://doi.org/10.1175/MWR3199.1>.
- James, R. P., and P. M. Markowski, 2010: A numerical investigation of the effects of dry air aloft on deep convection. *Mon. Wea. Rev.*, **138**, 140–161, <https://doi.org/10.1175/2009MWR3018.1>.
- Kain, J. S., 2004: The Kain-Fritsch convective parameterization: An update. *J. Appl. Meteor.*, **43**, 170–181, [https://doi.org/10.1175/1520-0450\(2004\)043<0170:TKCPAU>2.0.CO;2](https://doi.org/10.1175/1520-0450(2004)043<0170:TKCPAU>2.0.CO;2).
- Kilroy, G., and R. K. Smith, 2013: A numerical study of rotating convection during tropical cyclogenesis. *Q. J. R. Meteorol. Soc.*, **139**, 1255–1269, <https://doi.org/10.1002/qj.2022>.
- Kim, H. S., J. H. Kim, C. H. Ho, and P. S. Chu, 2011: Pattern classification of typhoon tracks using the fuzzy c-means clustering method. *J. Climate*, **24**, 488–508, <https://doi.org/10.1175/2010JCLI3751.1>.
- Komaromi, W. A., 2013: An investigation of composite dropsonde profiles for developing and nondeveloping tropical waves during the 2010 PREDICT field campaign. *J. Atmos. Sci.*, **70**, 542–558, <https://doi.org/10.1175/JAS-D-12-052.1>.
- Lau, K.-H., Z.-F. Zhang, H.-Y. Lam, and S.-Y. Chen, 2003: Numerical simulation of a South China Sea typhoon Leo (1999). *Meteor. Atmos. Phys.*, **83**, 147–161, <https://doi.org/10.1007/s00703-002-0559-5>.
- Montgomery, M. T., M. E. Nicholls, T. A. Cram, and A. B. Saunders, 2006: A vortical hot tower route to tropical cyclogenesis. *J. Atmos. Sci.*, **63**, 355–386, <https://doi.org/10.1175/JAS3604.1>.
- Nolan, D. S., 2007: What is the trigger for tropical cyclogenesis? *Aust. Meteor. Mag.*, **56**, 241–266.
- Park, M.-S., H.-S. Kim, C.-H. Ho, R. L. Elsberry, and M.-I. Lee, 2015: Tropical cyclone Mekkhala’s (2008) formation over the South China Sea: Mesoscale, synoptic-scale, and large-scale contributions. *Mon. Wea. Rev.*, **143**, 88–110, <https://doi.org/10.1175/MWR-D-14-00119.1>.
- Rappin, E. D., D. S. Nolan, and K. A. Emanuel, 2010: Thermodynamic control of tropical cyclogenesis in environments of radiative-convective equilibrium with shear. *Quart. J. Roy. Meteor. Soc.*, **136**, 1954–1971, <https://doi.org/10.1002/qj.706>.
- Raymond, D. D. J., C. López-Carrillo, and L. L. Cavazos, 1998: Case-studies of developing east Pacific easterly waves. *Quart. J. Roy. Meteor. Soc.*, **124**, 2005–2034, <https://doi.org/10.1002/qj.49712455011>.
- Rolph, G., A. Stein, and B. Stunder, 2017: Real-time environmental applications and display system: READY. *Environmental Modelling & Software*, **95**, 210–228, <https://doi.org/10.1016/j.envsoft.2017.06.025>.
- Rotunno, R., and K. A. Emanuel, 1987: An air-sea interaction theory for tropical cyclones. Part II: Evolutionary study using a nonhydrostatic axisymmetric numerical model. *J. Atmos. Sci.*, **44**, 542–561, [https://doi.org/10.1175/1520-0469\(1987\)044<0542:AAITFT>2.0.CO;2](https://doi.org/10.1175/1520-0469(1987)044<0542:AAITFT>2.0.CO;2).
- Smith, R. K., and M. T. Montgomery, 2012: Observations of the convective environment in developing and non-developing tropical disturbances. *Q. J. R. Meteorol. Soc.*, **138**, 1721–1739, <https://doi.org/10.1002/qj.1910>.
- Stein, A. F., R. R. Draxler, G. D. Rolph, B. J. B. Stunder, M. D. Cohen, and F. Ngan, 2015: NOAA’s HYSPLIT atmospheric transport and dispersion modeling system. *Bull. Amer. Meteor. Soc.*, **96**, 2059–2077, <https://doi.org/10.1175/BAMS-D-14-00110.1>.
- Tao, W.-K., J. Simpson, and M. McCumber, 1989: An ice-water saturation adjustment. *Mon. Wea. Rev.*, **117**, 231–235, [https://doi.org/10.1175/1520-0493\(1989\)117<0231:AIWSA>2.0.CO;2](https://doi.org/10.1175/1520-0493(1989)117<0231:AIWSA>2.0.CO;2).
- Tao, W.-K., J. Simpson, C. H. Sui, B. Ferrier, S. Lang, J. Scala, M. D. Chou, and K. Pickering, 1993: Heating, moisture, and water budgets of tropical and midlatitude squall lines: Comparisons and sensitivity to longwave radiation. *J. Atmos. Sci.*, **50**, 673–690, [https://doi.org/10.1175/1520-0469\(1993\)050<0673:HMAWBO>2.0.CO;2](https://doi.org/10.1175/1520-0469(1993)050<0673:HMAWBO>2.0.CO;2).
- Wang, L., R. H. Huang, and R. G. Wu, 2013: Interdecadal variability in tropical cyclone frequency over the South China Sea and its association with the Indian Ocean sea surface temperature. *Geophys. Res. Lett.*, **40**, 768–771, <https://doi.org/10.1002/grl.50171>.
- Wang, Y. P., X. P. Cui, X. F. Li, W. L. Zhang, and Y. J. Huang, 2016a: Kinetic energy budget during the genesis period of tropical cyclone Durian (2001) in the South China Sea. *Mon. Wea. Rev.*, **144**, 2831–2854, <https://doi.org/10.1175/MWR-D-15-0042.1>.
- Wang, Y. P., X. P. Cui, and Y. J. Huang, 2016b: Characteristics of multiscale vortices in the simulated formation of Typhoon Durian (2001). *Atmos. Sci. Lett.*, **17**, 492–500, <https://doi.org/10.1002/asl.683>.
- Wang, Z., 2012: Thermodynamic aspects of tropical cyclone formation. *J. Atmos. Sci.*, **69**, 2433–2451, <https://doi.org/10.1175/JAS-D-11-0298.1>.
- Wang, Z., M. T. Montgomery, and T. J. Dunkerton, 2010: Genesis of pre-hurricane Felix (2007). Part II: Warm core formation, precipitation evolution, and predictability. *J. Atmos. Sci.*, **67**, 1730–1744, <https://doi.org/10.1175/2010JAS3435.1>.
- Wu, L. G., 2007: Impact of Saharan air layer on hurricane peak intensity. *Geophys. Res. Lett.*, **34**, L09802, <https://doi.org/10.1029/2006GL027002>.

- 10.1029/2007GL029564.
- Yi, B. Q., A. K. H. Lau, A. M. Liang, and Q. H. Zhang, 2008: Numerical study of the genesis and development of typhoon Wukong (2000) over South China Sea. *Acta Scientiarum Naturalium Universitatis Pekinensis*, **44**, 773–780, <https://doi.org/10.3321/j.issn:0479-8023.2008.05.017>. (in Chinese)
- Yoshida, R., Y. Miyamoto, H. Tomita, and Y. Kajikawa, 2017: The effect of water vapor on tropical cyclone genesis: A numerical experiment of a non-developing disturbance observed in PALAU2010. *J. Meteor. Soc. Japan*, **95**, 35–47, <http://doi.org/10.2151/jmsj.2017-001>.
- Zawislak, J., and E. J. Zipser, 2014: Analysis of the thermodynamic properties of developing and nondeveloping tropical disturbances using a comprehensive dropsonde dataset. *Mon. Wea. Rev.*, **142**, 1250–1264, <https://doi.org/10.1175/MWR-D-13-00253.1>.
- Zhang, W., A. Wang, and X. Cui, 2008: The role of the middle tropospheric mesoscale convective vortex in the genesis of Typhoon Durian (2001)—Simulation and verification. *Chinese Journal of Atmospheric Sciences*, **32**, 1197–1209, <https://doi.org/10.3878/j.issn.1006-9895.2008.05.17>. (in Chinese)